

# Relation between Spherulitic Growth, Molecular Organization, and Charge Carrier Transport in Meniscus-Guided Coated Organic Semiconducting Films

Ke Zhang, Michal Borkowski, Philipp Wucher, Pierre M. Beaujuge, Jasper J. Michels, Paul. W. M. Blom, Tomasz Marszalek,\* and Wojciech Pisula\*

Meniscus-guided coating (MGC) is an efficient and promising route to grow small molecule and polymer organic semiconductors (OSCs) into highly ordered and uniaxially orientated thin films for electronic applications. In this work, the impact of domain size and molecular order on the charge carrier transport in field-effect transistors for a molecular organic semiconductor 4-tolyl-bithiophenyl-diketopyrrolopyrrole (DPP(Th<sub>2</sub>Bn)<sub>2</sub>) is investigated. The spherulitic domain growth of DPP(Th<sub>2</sub>Bn)<sub>2</sub> in thin films is controlled in the evaporative regime of zone-casting by varying the substrate velocity. The decrease of coating velocity leads to a lower nucleation density and larger domain size of DPP(Th<sub>2</sub>Bn)<sub>2</sub>. At sufficiently low velocity, the spherulitic domains first elongate and then uniaxially grow in the coating direction. Although at the same time the molecular order decreases due to higher film thickness, the charge carrier transport improves for larger domain size and reduced density of boundaries in the transistor channel. These results provide insight on the relation between domain growth, molecular organization, and charge carrier transport in zone-cast OSC thin films that are important for the upscaling of the technique for practical applications.


## 1. Introduction

Organic semiconductors (OSCs) have attracted great attention due to their mechanical flexibility and solution processability.<sup>[1,2]</sup> The performance of organic electronic devices strongly depends on molecular organization and morphology of the OSC in the deposited thin film.<sup>[3]</sup> Meniscus-guided coating (MGC) is a promising route to grow OSCs into highly ordered and long-range aligned crystalline films to ensure unhindered charge carrier transport and high performance of an electronic device.<sup>[4,5]</sup> Driven by the importance of controlling film morphology and molecular organization,<sup>[6]</sup> a number of MGC techniques, such as dip-coating,<sup>[7,8]</sup> zone-casting,<sup>[9,10]</sup> bar-coating,<sup>[11,12]</sup> and solution shearing,<sup>[13]</sup> have been developed over the last decade. The growth into long-range aligned structures has been achieved through MGC for liquid crystalline and crystalline small molecule OSCs.<sup>[9,13]</sup> High orientation of nanofibers

has been realized for conjugated polymers by dip-coating and bar-coating.<sup>[14]</sup>

Key processing parameters during MGC to control the film thickness and morphology are coating velocity ( $v$ ) and solvent evaporation rate.<sup>[15,16]</sup> MGC is characterized by two main regimes, namely evaporative regime and Landau–Levich regime, defined by the relation between film thickness and  $v$ . In the Landau–Levich regime a wet film is formed and subsequent solvent evaporation induces spatially random nucleation, upon which the thin film morphology forms by crystalline growth. In this regime, the film thickness increases as  $T \sim v^{2/3}$  due to a larger viscous drag at increasing speed. The reason for the exponent being smaller than unity stems from the super-linear decrease in momentum in the vertical direction, away from the substrate.<sup>[17]</sup> In the evaporative regime, the film thickness decreases as  $\sim v^{-1}$  as solvent evaporation from the meniscus drives mass transport toward the contact line at which the solidification of the solute takes place. Since the steady state evaporative flux does not depend on the coating velocity, mass conservation dictates that the entrainment rate should half, if the speed increases by a factor

Dr. K. Zhang, Dr. J. J. Michels, Prof. P. W. M. Blom, Dr. T. Marszalek, Prof. W. Pisula  
Max Planck Institute for Polymer Research  
Ackermannweg 10, Mainz 55128, Germany  
E-mail: marszalek@mpip-mainz.mpg.de; pisula@mpip-mainz.mpg.de  
M. Borkowski, Dr. T. Marszalek, Prof. W. Pisula  
Department of Molecular Physics  
Faculty of Chemistry  
Lodz University of Technology  
Zeromskiego 116, Lodz 90-924, Poland  
Dr. P. Wucher, Dr. P. M. Beaujuge  
Physical Sciences and Engineering Division  
KAUST Solar Center (KSC)  
King Abdullah University of Science and Technology (KAUST)  
Thuwal 23955-6900, Saudi Arabia

 The ORCID identification number(s) for the author(s) of this article can be found under <https://doi.org/10.1002/aelm.202100397>.

© 2021 The Authors. Advanced Electronic Materials published by Wiley-VCH GmbH. This is an open access article under the terms of the Creative Commons Attribution License, which permits use, distribution and reproduction in any medium, provided the original work is properly cited.

DOI: 10.1002/aelm.202100397

two. In the evaporative regime, crystal nucleation and growth occur exclusively in the vicinity of the contact line. At a certain  $v$  the formation of new nucleation sites is suppressed, while the crystallization and  $v$  are in correspondence leading to a directional growth of the domains. In this situation, a long-range orientation of the film structures without domain boundaries is achieved ensuring formation of optimal pathways for in-plane charge carrier transport.<sup>[18]</sup> Furthermore, the coating conditions can be adapted so that one polymorph can show different morphologies.<sup>[19]</sup>

Due to the significance of directionally oriented microstructure of thin films for the performance of organic field-effect transistors (OFETs), a comprehensive understanding on the relation between crystallization kinetics and processing conditions is mandatory. Therefore, many research reports focused on this aspect during the last years. A major factor for optimal film morphologies at steady-state processing conditions in the evaporative regime is the match between  $v$  and solvent evaporation rate, optimized for different small molecule OSCs, temperatures and solvents.<sup>[20,21]</sup> Superior morphology and electrical characteristics were also observed for zone-cast films when  $v$  was equal to the equilibrium front evaporation speed of the pure solvent.<sup>[22]</sup> At low  $v$ , supersaturation is no longer achieved after initial crystallization inducing aligned domain and molecular growth at optimized conditions. However, for faster  $v$ , an isotropic domain structure is expected due to supersaturation ahead of the growth front due to solvent evaporation as demonstrated by our recently reported modeling.<sup>[23]</sup> These coating conditions also result in higher molecular disorder because of a stochastic nucleation of crystallites.<sup>[24]</sup> Furthermore, crystal growth rate and film thickness are directly proportional to the concentration of the deposited solution.<sup>[25,26]</sup> But if  $v$  and evaporation rate are balanced, the crystallization of the organic semiconductor at the contact line and the resulting film morphology become independent of the solute concentration.<sup>[26]</sup> For the optimization of the deposition process, the flow dynamics in the meniscus has also to be taken into account. In the evaporative regime, the mass transport of molecules toward the contact line is crucial for the deposition rate and morphology formation of the film. A gradient of the surface tension at the meniscus can increase the molecular transport toward the deposition contact line area due to stronger Marangoni flow.<sup>[27]</sup> Another option to increase the mass transport is the addition of a small concentration of an amorphous polymer binder to the solution.<sup>[28]</sup> The subsequent higher and more homogenous film crystallinity during MGC is attributed to a viscosity gradient at the meniscus due to the binder facilitating the draw of solute and mass transport during coating. The mass transport during MGC is also controlled by the shape of the meniscus.

Dip-coating at a small meniscus angle enhances the mass deposition and crystallization of small molecules triggered by an enlarged upward fluid flow during coating.<sup>[29]</sup> The resulting aligned crystalline films show high surface coverage and charge carrier transport in OFETs. Another important aspect for the film crystallization during MGC is the surface energy of the substrate affecting the wetting of the solvent on the surface and contact line curvature.<sup>[15]</sup> Surface patterning into hydrophilic and hydrophobic areas allows selective deposition of the OSC

during MGC due to wetting and dewetting of the solution.<sup>[30]</sup> However, for low contact angles of the solution the morphology of zone-cast films was reported to be independent of the surface treatment.<sup>[31]</sup> This behavior was attributed to the rapid solvent evaporation and crystallization of the solute at the meniscus contact line during MGC.

In this work, the correlation between  $v$ , domain growth, long-range alignment, molecular order and charge carrier transport for MGC deposited small molecule OSC is established to determine the dominating factor for the electronic performance of transistors. Understanding the simultaneous influence of both parameters, domain size and molecular order, on charge carrier transport is an important aspect for the further development of MGC of next generation semiconductors. As model organic semiconductor, 4-tolyl-bithiophenyl-diketopyrrolopyrrole (DPP(Th<sub>2</sub>Bn)<sub>2</sub>) is chosen due its crystallization into distinct spherulitic domains. The growth into spherulites is beneficial since it allows to tune solely the domain size by the processing parameters without changing the crystal morphology. The film deposition was performed by zone-casting at varying  $v$  and constant processing temperature to adjust the domain size. At sufficiently low  $v$  the domains are stretched in the casting direction until a homogenous long-range alignment without boundaries is reached. The structural analysis confirmed a molecular orientation in the oriented crystalline films, but at the same time a lowered molecular order. Although the molecular order decreases, as the main structural parameter, the charge carrier transport is improved with larger domains and reduced density of boundaries in the transistor channel. This work provides novel insight in the correlation between domain growth, molecular order and charge carrier transport in OSC films obtained by zone-casting and provides essential guidelines for future scaling-up MGC techniques for manufacturing large-area organic electronics.

## 2. Results and Discussion

DPP(Th<sub>2</sub>Bn)<sub>2</sub> consists of a conjugated diketopyrrolopyrrole and thiophene oligomer backbone and was deposited at different  $v$  by zone-casting as illustrated in **Figure 1a**. The corresponding film morphologies were first inspected by polarized optical (POM) and atomic force microscopies (AFM) (**Figure 1c,d**). For all studied  $v$ , a continuous crystalline film composed of densely packed DPP(Th<sub>2</sub>Bn)<sub>2</sub> spherulites is observed. The casting conditions were chosen not to affect the fluid dynamics. Therefore, only changes in size and orientation of the spherulitic domains are observed as consequence of variation of  $v$ . To obtain the relation between mean domain size ( $A_v$ ) and  $v$ , the domain boundaries were highlighted in POM images and extracted into domain contour images (**Figure S1**, Supporting Information) allowing to present  $A_v$  as a function of  $v$  in **Figure 1b**. As evident from the POM and AFM images, the film morphology for 500 and 1000  $\mu\text{m s}^{-1}$  consists of isotropic impinged spherulitic domains, nucleated randomly across the film. Relatively small DPP(Th<sub>2</sub>Bn)<sub>2</sub> domains of  $A_{1000} \approx 30 \mu\text{m}^2$  are obtained at 1000  $\mu\text{m s}^{-1}$ . When  $v$  is decreased from 1000 to 75  $\mu\text{m s}^{-1}$ , the average size of the DPP(Th<sub>2</sub>Bn)<sub>2</sub> domains significantly increases. At low  $v$  of 75  $\mu\text{m s}^{-1}$ ,  $A_{75}$  reaches a size

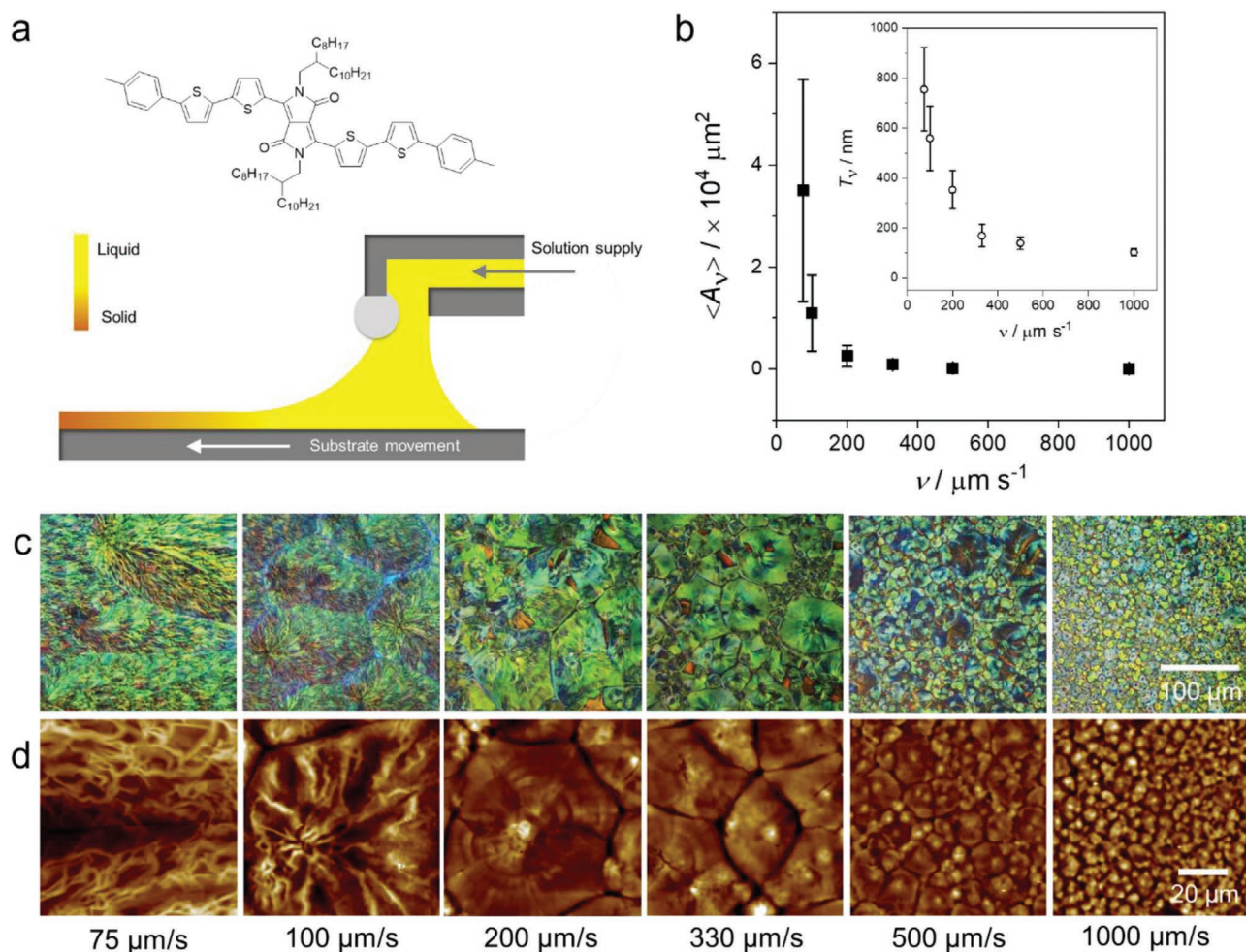


**Figure 1.** a) Schematic illustration of zone-casting and molecule structure of DPP(Th<sub>2</sub>Bn)<sub>2</sub>, b) relation between  $A_v$  and  $\nu$  for zone-cast DPP(Th<sub>2</sub>Bn)<sub>2</sub> (inset:  $T_v$  as a function of  $\nu$ ), c) POM, and d) AFM images of zone-cast DPP(Th<sub>2</sub>Bn)<sub>2</sub> domains obtained at different  $\nu$ .

of 30000  $\mu\text{m}^2$ , around 1000 times of  $A_{1000}$ . With decreasing  $\nu$ , the domains become anisotropic (Figure 1c,d) as recently predicted by our model.<sup>[23]</sup> At 75 and 100  $\mu\text{m s}^{-1}$ , the domains exhibit a preferred directionality along the casting direction. At these velocities, the nucleation point is off-centered within the elongated domains, differently from the central nucleation at 500 and 1000  $\mu\text{m s}^{-1}$  (Figure 1d). The model has exposed that at high coating velocity, solute depletion from the solution due to solidification is overcompensated by accumulation leading to an isotropic domain shape. The depletion dominates at a low velocity and prevents collision of the growth front onto newly nucleated crystallites resulting in the formation of stretched domains.<sup>[23]</sup>

The mean thickness ( $T_v$ ) of the DPP(Th<sub>2</sub>Bn)<sub>2</sub> films is much smaller than the mean diameter ( $d_v$ ) of the domains, especially for low  $\nu$ . The parameter  $T_v$  also exhibits a pronounced rise with the decrease of  $\nu$ , as shown in the inset of Figure 1b. For instance,  $T_{75}$  of 750 nm at 75  $\mu\text{m s}^{-1}$  is around 7 times higher than  $T_{1000}$  at 1000  $\mu\text{m s}^{-1}$  and is determined by the deposited mass per area at a specific substrate speed (inset in Figure 1b).

### 3. Molecular Organization

To investigate the molecular order and long-range orientation in the zone-cast films, grazing incidence wide-angle X-ray scattering (GIWAXS) was employed. The analysis of the structural data reveals that the coating speed does not affect the lattice parameters of DPP(Th<sub>2</sub>Bn)<sub>2</sub>, but strongly influences the domain size and directional molecular alignment in the film. All deposited films show an edge-on orientation of the DPP(Th<sub>2</sub>Bn)<sub>2</sub> molecules as evident from the out-of-plane position of the (100) reflection corresponding to the interlayer distance of 2.10 nm (Figure 2a). The off position of the  $\pi$ -stacking reflection, as indicated in the inset of Figure 2d and assigned to the distance of 0.36 nm, additionally suggests a 32° tilting of the molecules toward the substrate. Measurements performed with the incident beam perpendicular and parallel to the casting direction provide information about the structural anisotropy as a function of  $\nu$ . The DPP(Th<sub>2</sub>Bn)<sub>2</sub> film cast at the highest  $\nu$  of 1000  $\mu\text{m s}^{-1}$  exhibits identical reflection patterns for the parallel and perpendicular measurements (Figure S2, Supporting Information), corresponding to the small and isotropically shaped

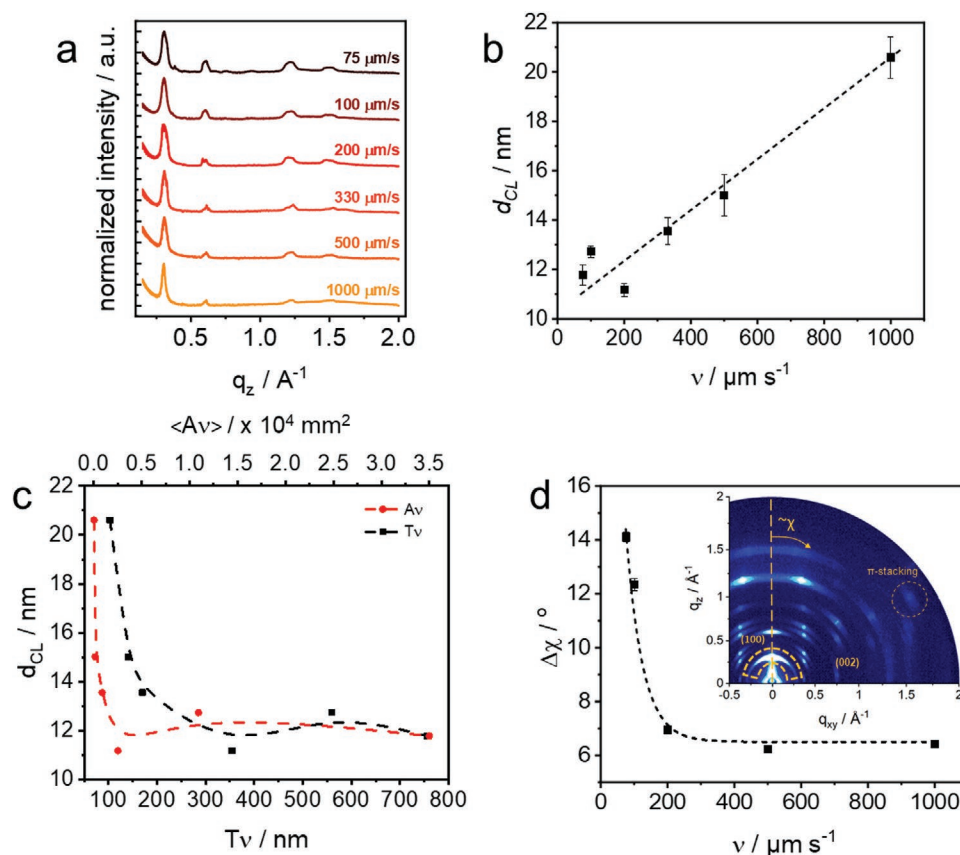


**Figure 2.** a) Out-of-plane parallel GIWAXS profiles for DPP(Th<sub>2</sub>Bn)<sub>2</sub> zone-cast at different  $v$ ; b) coherence length  $d_{\text{CL}}$  calculated for the (100) reflection as a function of  $v$ ; and c)  $d_{\text{CL}}$  as a function of  $A_v$  and  $T_v$ ; d) FWHM for the angular distribution of (100) reflection parallel to coating direction (inset: GIWAXS pattern recorded in the parallel direction for DPP(Th<sub>2</sub>Bn)<sub>2</sub> zone-cast at 75  $\mu\text{m s}^{-1}$ , main reflections used for the structural analysis are indicated. All dashed lines in the graphs are eye guides.

domains observed by POM and AFM. In contrast, scattering patterns in Figure S2 (Supporting Information) recorded for the perpendicular and parallel coating directions differ for the film deposited at lowest  $v$  of 75  $\mu\text{m s}^{-1}$  confirming an orientation at a molecular level that persists in the elongated domains across a macroscopic length scale.

The structural anisotropy is derived for different  $v$  and the parallel and perpendicular directions of the film orientation from the intensity ratio  $I_{\perp}:I_{\parallel}$  of the in-plane (002) reflection (as indicated in the inset pattern in Figure 2d). The highest  $I_{\perp}:I_{\parallel}$  ratio of 1.3 is determined for the lowest  $v$  of 75  $\mu\text{m s}^{-1}$ , while for highest  $v$  of 1000  $\mu\text{m s}^{-1}$  this value drops to near unity. Due to the weak scattering of the zone-cast films, the out-of-plane interlayer 100 reflection was used to calculate the coherence length ( $d_{\text{CL}}$ ) to indicate changes in molecular order as function of  $v$ . The out-of-plane  $d_{\text{CL}}$  linearly increases with higher  $v$  from 11.8 nm at 75  $\mu\text{m s}^{-1}$  to 20.6 nm at 1000  $\mu\text{m s}^{-1}$  (Figure 2b). At the same time,  $d_{\text{CL}}$  declines with the film thickness and in-plane domain size  $A_v$  as shown in Figure 2c. These correlations prove that the crystallinity is reduced for higher film thickness despite of an in-plane directional growth of the domains indicating a pronounced impact of the substrate surface on the molecular ordering in thinner films.

As another structural parameter, the uniformity of the crystallite arrangement with respect to the substrate is characterized

by the full width at half maximum (FWHM)  $\chi$  extracted from the angular intensity distribution of the (100) out-of-plane reflection from the parallel GIWAXS patterns (Figure 2d). This value decreases from 14.1° for films coated at 75  $\mu\text{m s}^{-1}$  to 7.6° for 200  $\mu\text{m s}^{-1}$  and remains on a constant level for higher  $v$  (Figure 2d). Both parameters  $\chi$  and  $A_v$  are closely linked to each other and follow the same trend with  $v$ . The lower  $\chi$  and  $d_{\text{CL}}$  values for higher  $v$  confirm an increased molecular ordering for smaller film thickness. The higher crystallinity found for thinner films is attributed to surface induced and confined crystallization. For thicker film, the role of the surface becomes smaller and the film bulk exhibits lower molecular order despite long-range alignment of the domains in the coating direction.

#### 4. Electronic Performance

The influence of domain size and directionality on charge carrier mobility ( $\mu_v$ ) in zone-cast films of DPP(Th<sub>2</sub>Bn)<sub>2</sub> was investigated by fabricating FETs in bottom-gate/top-contact (BGTC) configuration. The BGTC configuration excludes an influence of the bottom electrodes on the crystal growth of the OSC. Furthermore, it typically leads to an underestimated  $\mu_v$  induced by bulk traps for thick film,<sup>[32]</sup> since the effective pathways for charge carriers in the transistor are formed by the first few

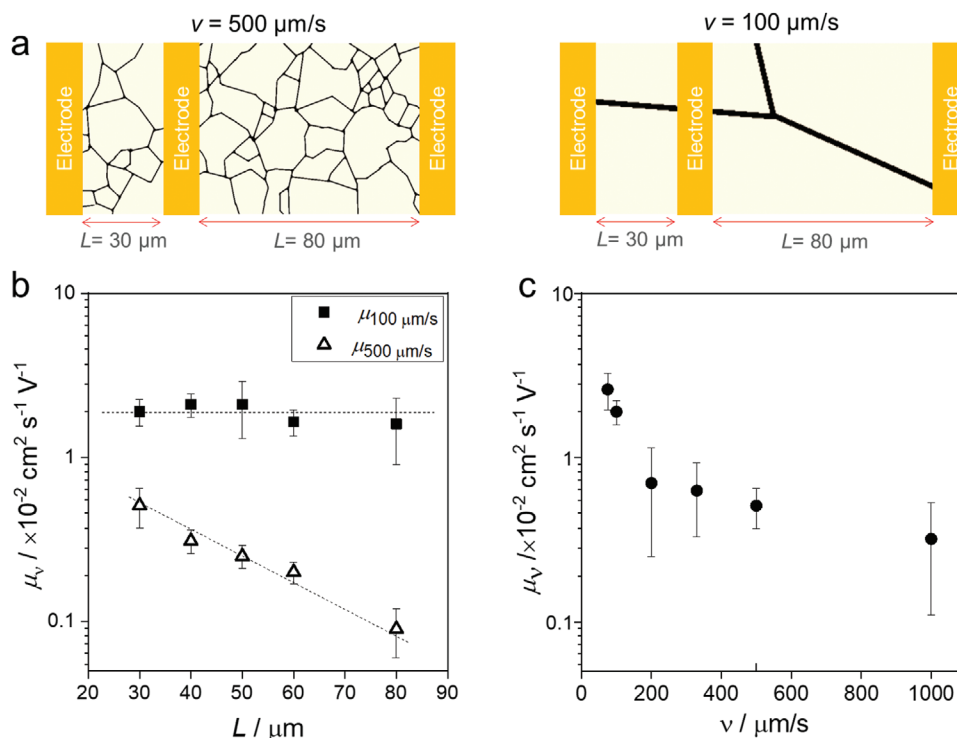


**Figure 3.** a) Illustration of domain boundaries between source and drain electrode for DPP(Th<sub>2</sub>Bn)<sub>2</sub> films zone-cast at 100 and 500  $\mu\text{m s}^{-1}$ , b)  $\mu_v$  as a function of  $L$  for films zone-cast at 100 and 500  $\mu\text{m s}^{-1}$ , and c)  $\mu_v$  as a function of  $v$  at  $L = 30 \mu\text{m}$ .

layers at the interface to the dielectric.<sup>[33]</sup> We note that since this work focuses on the effect of the crystal growth of the organic semiconductor as a function of the coating speed, process optimization toward high FET performance is considered out of scope.

The devices show a typical p-type behavior that is strongly dependent on  $v$  and channel length ( $L$ ) of the device. In films cast at 500  $\mu\text{m s}^{-1}$ ,  $d_{500}$  of the DPP(Th<sub>2</sub>Bn)<sub>2</sub> domains is smaller than  $L$  of the transistor (Figure 3a). For transistors with  $L_{30\mu\text{m}}$ ,  $\mu_{500\mu\text{m/s}}$  is around  $5.1 \times 10^{-3} \text{ cm}^2 \text{ s}^{-1} \text{ V}^{-1}$ , with an on/off ratio around 5000 (Figure S3a, Supporting Information). With the increase of  $L$ ,  $\mu_{500\mu\text{m/s}}$  decreases linearly to  $0.9 \times 10^{-3} \text{ cm}^2 \text{ s}^{-1} \text{ V}^{-1}$  for  $L_{80\mu\text{m}}$  (Figure 3b). The mobility  $\mu_{500\mu\text{m/s}}$  is linearly dependent on  $L$  due to the small domain size. As schematically shown in Figure 3a for the film cast at 500  $\mu\text{m s}^{-1}$ , the number of domain boundaries as trapping sites between source and drain electrodes greatly increases when  $L$  is enlarged from 30 to 80  $\mu\text{m}$ . In contrast,  $\mu_{100\mu\text{m/s}}$  remains constant between  $1.6\text{--}2.1 \times 10^{-2} \text{ cm}^2 \text{ s}^{-1} \text{ V}^{-1}$  for  $L$  in the range of 30–80  $\mu\text{m}$ , (Figure 3b and Figure S3c, Supporting Information). The  $L$ -independent  $\mu_{100\mu\text{m/s}}$  is attributed to the much larger domains which are comparable to or larger than  $L$  (Figure 3a).

Figure 3c presents the relation between  $\mu_v$  and  $v$  for zone-cast DPP(Th<sub>2</sub>Bn)<sub>2</sub> transistors with  $L_{30\mu\text{m}}$ . When  $v$  decreases from 1000 to 200  $\mu\text{m s}^{-1}$ ,  $\mu_v$  increases only slightly from  $0.3 \times 10^{-2}$  to  $0.7 \times 10^{-2} \text{ cm}^2 \text{ s}^{-1} \text{ V}^{-1}$ , while for lower  $v$  of 100 and 75  $\mu\text{m s}^{-1}$ ,  $\mu_{100\mu\text{m/s}}$  and  $\mu_{75\mu\text{m/s}}$  increase to  $1.9 \times 10^{-2}$  and  $2.7 \times 10^{-2} \text{ cm}^2 \text{ s}^{-1} \text{ V}^{-1}$ , respectively (Figure 3c and Figure S3e, Supporting Information). Despite the improvement of the charge carrier mobility, the output curves for  $v$  of 100 and 75  $\mu\text{m s}^{-1}$  in

Figure S3e (Supporting Information) indicate contact and bulk resistance due to a rougher semiconductor/electrode interface of the large DPP(Th<sub>2</sub>Bn)<sub>2</sub> domains and higher film thickness. The overall upward trend of  $\mu_v$  with lower  $v$  follows the rise of  $A_v$ , despite the decreased molecular order and higher bulk resistance (Figure 3c). As evident from Figure S4 (Supporting Information), the charge carrier mobility increases with higher azimuthal crystal misalignment and lower coherence length. At the same time, as presented in Figures 1b and 3c, the mobility rises with the increase in domain size obtained at lower coating velocity. From these correlations, it can be concluded that the influence of molecular disorder on charge carrier mobility is overcompensated by the increase of the domain size. Therefore, a larger size and a preferential orientation of the domains are the dominating factors for the improvement of the charge carrier transport in the zone-cast DPP(Th<sub>2</sub>Bn)<sub>2</sub> films ( $\mu_{75\mu\text{m/s}}$  is around 9 times higher than  $\mu_{1000\mu\text{m/s}}$ ).

## 5. Conclusion

In this work, the crystal growth and morphology formation of DPP(Th<sub>2</sub>Bn)<sub>2</sub> as model organic semiconductor for spherulitic domains during MGC is investigated. The spherulitic domain size of DPP(Th<sub>2</sub>Bn)<sub>2</sub> is controlled by the coating velocity ( $v$ ) during zone-casting, whereby a low  $v$  leads to large size and directional growth of the domains. The slower  $v$  ensures a low nucleation density, large and off-centered nucleation resulting in domains becoming stretched in the coating direction with a low density of domain boundaries. At the same time, with

reducing  $v$  and increasing  $T_v$ , the molecular order declines as consequence of the higher film thickness. As the dominating factor for the charge carrier transport in transistors, the conduction pathways are established for domain sizes exceeding the channel length of the device overcompensating the decreased molecular order and higher bulk resistance. In this way, the density of domain boundaries within the transistor channel is restrained. The found correlations are crucial for the development of MGC as a practical processing technique for upscaling the solution deposition of organic semiconductors in future.

## 6. Experimental Section

**Meniscus-Guided Coating:** Silicon substrate with a 300 nm SiO<sub>2</sub> layer was treated by oxygen plasma for 3 min. Zone-casting was performed from 3 mg mL<sup>-1</sup> DPP(Th<sub>2</sub>Bn)<sub>2</sub>/CHCl<sub>3</sub> solution on silicon substrate with varying coating velocities from 75 to 1000 μm s<sup>-1</sup>. During zone-casting, the solution and substrate temperatures were 50 °C.

**Characterization Methods:** POM images were obtained by Leica polarized optical microscope at partly polarized condition to gain a distinct contrast of the domain boundaries. Domain boundaries were highlighted on the POM images by Adobe Photoshop CS6, and then the domain contour images were extracted. Domain sizes were calculated from domain contour images by ImageJ. The thickness of DPP(Th<sub>2</sub>Bn)<sub>2</sub> crystalline films was determined with a P-7 stylus profiler (KLA Tencor). GIWAXS measurements were performed by means of a solid anode X-ray tube (Seimens Kristalloflex X-ray source, copper anode X-ray tube operated at 35 kV and 40 mA), Osmic confocal MaxFlux optics, X-ray beam with pinhole collimation, and an MAR345 image plate detector calibrated with the usage of silver behenate. Datasqueeze software was used for data processing and analysis. The coherence length was determined using the Scherrer equation<sup>[34]</sup>

$$d_{CL} = \frac{2\pi K}{\Delta q} \quad (1)$$

where  $\Delta q$  is the full width at half-maximum of the reflection and  $K$  is a shape factor with the empirical value of 0.9. Reflections were fitted to Lorentz distribution with usage of Origin 2018 software. Errors of estimate were determined by exact differential method.

**OFET Characterization:** Bottom-gate/top contact configuration devices were fabricated to reveal the influence of domain size on the charge transport. Heavily n-type doped Si wafers were used as gate electrode and the 300 nm SiO<sub>2</sub> layer (11 nF cm<sup>-2</sup>) acted as a gate dielectric. DPP(Th<sub>2</sub>Bn)<sub>2</sub> crystalline films were annealed at 100 °C in glove box for 1 h to remove residual solvent. Source and drain electrodes were deposited at a thickness of 50 nm by gold thermal evaporation. The transistor channel width is 1000 μm with the channel lengths varying from 30 to 80 μm. A Keithley 4200-SCS was used for measurements of the charge transport in glove box under nitrogen atmosphere.

## Supporting Information

Supporting Information is available from the Wiley Online Library or from the author.

## Acknowledgements

K.Z. thanks the China Scholarship Council (CSC) for financial support. M.B. and T.M. acknowledge the Foundation for Polish Science financed by the European Union under the European Regional Development Fund (POIR.04.04.00-00-3ED8/17). W.P. acknowledges the National

Science Centre, Poland through grants UMO-2015/18/E/ST3/00322 and UMO-2019/33/B/ST3/1550.

Open access funding enabled and organized by Projekt DEAL.

## Conflict of Interest

The authors declare no conflict of interest.

## Data Availability Statement

Research data are not shared.

## Keywords

charge carrier transport, domain growth, field-effect transistor, meniscus-guided coating, organic semiconductor

Received: April 17, 2021

Revised: May 20, 2021

Published online: June 23, 2021

- [1] J. Y. Oh, S. Rondeau-Gagne, Y. C. Chiu, A. Chortos, F. Lissel, G. N. Wang, B. C. Schroeder, T. Kurosawa, J. Lopez, T. Katsumata, J. Xu, C. Zhu, X. Gu, W. G. Bae, Y. Kim, L. Jin, J. W. Chung, J. B. Tok, Z. Bao, *Nature* **2016**, 539, 411.
- [2] S. Wang, J. Xu, W. Wang, G. N. Wang, R. Rastak, F. Molina-Lopez, J. W. Chung, S. Niu, V. R. Feig, J. Lopez, T. Lei, S. K. Kwon, Y. Kim, A. M. Foudeh, A. Ehrlich, A. Gasperini, Y. Yun, B. Murmann, J. B. Tok, Z. Bao, *Nature* **2018**, 555, 83.
- [3] Y. Diao, L. Shaw, Z. Bao, S. C. B. Mannsfeld, *Energy Environ. Sci.* **2014**, 7, 2145.
- [4] X. Gu, L. Shaw, K. Gu, M. F. Toney, Z. Bao, *Nat. Commun.* **2018**, 9, 534.
- [5] M. Chang, G. Lim, B. Park, E. Reichmanis, *Polymers* **2017**, 9, 212.
- [6] G. De Luca, W. Pisula, D. Credgington, E. Treossi, O. Fenwick, G. M. Lazzarini, R. Dabirian, E. Orgiu, A. Liscio, V. Palermo, K. Müllen, F. Cacialli, P. Samori, *Adv. Funct. Mater.* **2011**, 21, 1279.
- [7] L. Li, P. Gao, W. Wang, K. Müllen, H. Fuchs, L. Chi, *Angew. Chem., Int. Ed. Engl.* **2013**, 52, 12530.
- [8] W. Deng, X. Zhang, H. Dong, J. Jie, X. Xu, J. Liu, L. He, L. Xu, W. Hu, X. Zhang, *Mater. Today* **2019**, 24, 17.
- [9] W. Pisula, A. Menon, M. Stepputat, I. Lieberwirth, U. Kolb, A. Tracz, H. Sirringhaus, T. Pakula, K. Müllen, *Adv. Mater.* **2005**, 17, 684.
- [10] Y. Su, X. Gao, J. Liu, R. Xing, Y. Han, *Phys. Chem. Chem. Phys.* **2013**, 15, 14396.
- [11] D. Khim, H. Han, K. J. Baeg, J. Kim, S. W. Kwak, D. Y. Kim, Y. Y. Noh, *Adv. Mater.* **2013**, 25, 4302.
- [12] J. Bai, Y. Jiang, Z. Wang, Y. Sui, Y. Deng, Y. Han, Y. Geng, *Adv. Electron. Mater.* **2020**, 6, 1901002.
- [13] Y. Diao, B. C. Tee, G. Giri, J. Xu, H. Kim do, H. A. Becerril, R. M. Stoltenberg, T. H. Lee, G. Xue, S. C. Mannsfeld, Z. Bao, *Nat. Mater.* **2013**, 12, 665.
- [14] a) S. Wang, A. Kiersnowski, W. Pisula, K. Müllen, *J. Am. Chem. Soc.* **2012**, 134, 4015; b) S. Wang, M. Kivala, I. Lieberwirth, K. Kirchoff, X. Feng, W. Pisula, K. Müllen, *ChemPhysChem* **2011**, 12, 1648.
- [15] B. B. Patel, Y. Diao, *Nanotechnology* **2018**, 29, 044004.
- [16] M. Richard, A. Al-Ajaji, S. Ren, A. Foti, J. Tran, M. Frigoli, B. Gusarov, Y. Bonnassieux, E. G. Caurel, P. Bulkin, R. Ossikovski, A. Yassar, *Adv. Colloid Interface Sci.* **2020**, 275, 102080.
- [17] a) L. Landau, B. G. Levich, *Acta Physicochim. URSS* **1942**, 17, 42; b) B. C. R. Deryaguin, *Acad. Sci. USSR* **1943**, 39, 13.

- [18] Z. Lu, C. Wang, W. Deng, M. T. Achille, J. Jie, X. Zhang, *J. Mater. Chem. C* **2020**, *8*, 9133.
- [19] A. Tamayo, S. Riera-Galindo, A. O. F. Jones, R. Resel, M. Mas-Torrent, *Adv. Mater. Interfaces* **2019**, *6*, 1900950.
- [20] J. Jang, S. Nam, K. Im, J. Hur, S. N. Cha, J. Kim, H. B. Son, H. Suh, M. A. Loth, J. E. Anthony, J.-J. Park, C. E. Park, J. M. Kim, K. Kim, *Adv. Funct. Mater.* **2012**, *22*, 1005.
- [21] C. W. Sele, B. K. Kjellander, B. Niesen, M. J. Thornton, J. B. van der Putten, K. Myny, H. J. Wondergem, A. Moser, R. Resel, A. J. van Breemen, N. van Aerle, P. Heremans, J. E. Anthony, G. H. Gelinck, *Adv. Mater.* **2009**, *21*, 4926.
- [22] R. Janneck, F. Vercesi, P. Heremans, J. Genoe, C. Rolin, *Adv. Mater.* **2016**, *28*, 8007.
- [23] J. J. Michels, K. Zhang, P. Wucher, P. M. Beaujuge, W. Pisula, T. Marszalek, *Nat. Mater.* **2021**, *20*, 68.
- [24] L. Shaw, H. Yan, X. Gu, P. Hayoz, R. T. Weitz, D. Kaelblein, M. F. Toney, Z. Bao, *Macromolecules* **2018**, *51*, 4325.
- [25] M. Chen, B. Peng, S. Huang, P. K. L. Chan, *Adv. Funct. Mater.* **2020**, *30*, 1905963.
- [26] R. Janneck, D. Karagiannis, P. Heremans, J. Genoe, C. Rolin, *Adv. Mater. Interfaces* **2019**, *6*, 1900614.
- [27] Z. Zhang, B. Peng, X. Ji, K. Pei, P. K. L. Chan, *Adv. Funct. Mater.* **2017**, *27*, 1703443.
- [28] K. Zhang, T. Marszalek, P. Wucher, Z. Wang, L. Veith, H. Lu, H.-J. Räder, P. M. Beaujuge, P. W. M. Blom, W. Pisula, *Adv. Funct. Mater.* **2018**, *28*, 1805594.
- [29] K. Zhang, Z. Wang, T. Marszalek, M. Borkowski, G. Fytas, P. W. M. Blom, W. Pisula, *Mater. Horiz.* **2020**, *7*, 1631.
- [30] D.-K. Kim, P. Vincent, J. Jang, I. M. Kang, H. Kim, P. Lang, M. Choi, J.-H. Bae, *Appl. Surf. Sci.* **2020**, *504*, 144362.
- [31] R. Janneck, P. Heremans, J. Genoe, C. Rolin, *Adv. Mater. Interfaces* **2018**, *5*, 1800147.
- [32] D. Gupta, Y. Hong, *Org. Electron.* **2010**, *11*, 127.
- [33] F. Dinelli, M. Murgia, P. Levy, M. Cavallini, F. Biscarini, D. M. de Leeuw, *Phys. Rev. Lett.* **2004**, *92*, 116802.
- [34] J. Rivnay, S. C. Mannsfeld, C. E. Miller, A. Salleo, M. F. Toney, *Chem. Rev.* **2012**, *112*, 5488.